



室蘭工業大学

学術資源アーカイブ

Muroran Institute of Technology Academic Resources Archive



Effect of Co Doping on the Structure and Magnetic Properties of $TmMn_{1-x}Co_xO_3$

メタデータ	言語: eng 出版者: The Physical Society of Japan 公開日: 2019-07-01 キーワード (Ja): キーワード (En): 作成者: 坂爪, 康則, バオ, ジンファ, 大杉, 駿介, 雨海, 有佑, 高野, 英明 メールアドレス: 所属:
URL	http://hdl.handle.net/10258/00009943

Effect of Co Doping on the Structure and Magnetic Properties of $\text{TmMn}_{1-x}\text{Co}_x\text{O}_3$

Yasunori Sakatsume, JianHua Bao, Shunsuke Ohsugi,
Yusuke Amakai, and Hideaki Takano*

*Graduate School of Engineering, Muroran Institute of Technology,
27-1 Mizumoto-cho, Muroran, Hokkaido 050-8585, Japan*

(Received)

We report the structure and magnetic properties of Co-doped TmMnO_3 polycrystals for Co doping levels of $0 \leq x \leq 0.9$. TmMnO_3 ($x=0$) prepared at ambient pressure was hexagonal. Hexagonal and orthorhombic phases coexisted in $\text{TmMn}_{1-x}\text{Co}_x\text{O}_3$ for $0 \leq x < 0.5$. We obtained almost single-phase orthorhombic samples with $0.5 \leq x \leq 0.9$ using complex polymerization. Ferromagnetic orthorhombic $\text{TmMn}_{1-x}\text{Co}_x\text{O}_3$ formed upon Co doping. The ionic states of Tm, Mn, and Co were determined through magnetization measurements. The rapid decrease in magnetization for $0.5 \leq x \leq 0.7$ below about 25 K was explained using a model consisting of a combination of ferromagnetic Mn-Co and paramagnetic Tm sublattices.

*E-mail: takano@mmm.muroran-it.ac.jp

1. Introduction

The manganese rare-earth oxide RMnO_3 has been investigated extensively because of its diverse physical properties and potential applications.¹⁻⁴⁾ Moreover, detailed studies on R-site and Mn-site substitutions have been carried out.⁵⁻⁸⁾ Upon the substitution of R with divalent elements such as Sr and Ca, and of Mn with other transition metals such as Co, Ni, and Cr, the valence of Mn partially changes from Mn^{3+} to Mn^{4+} , and the system undergoes various exchange interactions. In particular, during Co substitutions involving multiple valence states, exchange interactions among Mn^{3+} , Mn^{4+} , Co^{2+} , and Co^{3+} can be expected depending on the amount of Co substitution, and the physical properties generated by the various interactions are very interesting.

It has been reported that in hexagonal TmMnO_3 , an antiferromagnetic spin ordering ($T_N \approx 82\text{-}86$ K) and a ferroelectric ordering of charges (ferroelectric Curie temperature $T_{\text{EC}} \approx 570\text{-}593$ K) may coexist.⁹⁻¹¹⁾ On the other hand, TmMnO_3 synthesized under high pressure is orthorhombic and antiferromagnetic with a Neel temperature of 41 K and a dielectric Curie temperature of about 32 K.^{12,13)} The antiferromagnetic state of this system is due to the exchange interaction between Mn^{3+} ions. By realizing a mixed-valence state of Mn by replacing the Tm and/or Mn of TmMnO_3 , it is possible to introduce a new factor into the magnetic behavior of the system. To investigate the effects of Co doping on the physical properties of TmMnO_3 , we substituted Mn with Co and studied the structure and magnetic properties of $\text{TmMn}_{1-x}\text{Co}_x\text{O}_3$. In $\text{TmMn}_{1-x}\text{Co}_x\text{O}_3$ prepared by a solid-phase reaction, the substitution of Mn with Co induced a hexagonal-to-orthorhombic transformation for $0 \leq x \leq 0.5$, and the samples with $x \geq 0.4$ became almost single-phase orthorhombic.¹⁴⁾ In the Co-substituted system, the magnetization increased ferromagnetically at about 60 K with decreasing temperature, and had a maximum at around 30 K. The maximum magnetization increased with x for $0 \leq x \leq 0.5$. For $x \geq 0.5$, the amount of Tm_2O_3 impurity increased with x . The presence of this impurity made the quantitative analysis of the data difficult. In this paper, we present a new synthesis method for $\text{TmMn}_{1-x}\text{Co}_x\text{O}_3$ and describe its structure and magnetic properties.

2. Experimental Procedure

Polycrystalline $\text{TmMn}_{1-x}\text{Co}_x\text{O}_3$ ($0 \leq x \leq 0.9$) compounds were prepared by a conventional solid-state reaction (SSR) and complex polymerization (CP).^{15,16)} All processes were performed at ambient pressure except for the pelletization of the mixture. In the SSR method, appropriate amounts of Tm_2O_3 , Mn_2O_3 , and Co_3O_4 , all of which were of 99.9% purity, were dried at 473 K.

These powders were ground, thoroughly mixed, and sintered at 1423 K under an O₂ atmosphere. Then, the mixtures were ground again and pelletized at 500 kgf/cm². These pellets were sintered at 1423 K under O₂. The starting materials used in the CP method were the metal nitrate hydrates Tm(NO₃)₂·4H₂O, Mn(NO₃)₂·6H₂O, and Co(NO₃)₂·4H₂O, which were of 99.9% purity. These nitrates were dissolved in water and mixed with a citric acid solution. After sufficient stirring, the solution was polymerized using ethylene glycol to form a transparent polymeric gel. The temperature range for gel formation was 463 to 493 K. The gel, which was dried at 623 - 673 K on a hot plate, became a resin. This resin was easily pulverized in an agate mortar. The powder was pelletized and sintered below 1273 K under an O₂ atmosphere. The pelletization and sintering processes were repeated several times. For $x < 0.5$, both the conventional SSR and CP methods were used. Quantitative differences due to sample preparation were minimal, and similar results have been reported previously.¹⁴⁾ For $0.5 \leq x \leq 0.9$, the CP method was used.

The crystal phases were analyzed using a MiniFlex 300 (Rigaku Co.) diffractometer with a Cu X-ray tube, a one-dimensional detector, and a Ni-K β filter. Structural analysis was conducted by Rietveld refinement using the software RIETAN-FP.¹⁷⁾ The magnetization measurements were performed with a superconducting quantum interference device (SQUID) magnetometer (Quantum Design).

3. Results and Discussion

3.1 Structure

Figure 1 shows typical X-ray diffraction (XRD) patterns for TmMn_{1-x}Co_xO₃ prepared by CP, with the XRD pattern for Tm₂O₃ included as a reference. TmMnO₃ ($x=0$), which was prepared at ambient pressure by the SSR, was hexagonal. These XRD patterns were refined by Rietveld analysis, and we obtained the lattice parameters a , b , c and the unit cell volume V in Fig. 2, along with the mass fraction of the hexagonal and orthorhombic phases shown in the inset, all as functions of x . The inset in Fig. 3 shows the mass fraction of the components of the SSR samples. Hexagonal and orthorhombic phases coexist for $0 < x < 0.5$ in samples prepared by either the SSR or CP. For $0.5 \leq x \leq 0.9$, the CP samples are almost single-phase orthorhombic, while the SSR samples contain a small amount of Tm₂O₃. The amount of this impurity in the SSR samples increases with increasing x . This indicates that the CP method is superior to the SSR method for the synthesis of samples with $0.5 < x \leq 0.9$. The space group for the hexagonal phase is P6₃cm, and the orthorhombic phase is a distorted perovskite with the space group Pnma. The lattice parameters a_h , c_h , and V_h in the hexagonal phase are nearly constant except for the case of $x=0.4$.

It is considered that the discrepancies for $x=0.4$ are caused by errors due to the small mass fraction of the hexagonal phase. The lattice parameters a_o , b_o , c_o , and V_o for the orthorhombic phase decrease with increasing x for $0.5 \leq x \leq 0.9$. This is presumably related to the ionic radii in $\text{TmMn}_{1-x}\text{Co}_x\text{O}_3$. Peña et al. suggested that for $\text{ErMe}_x\text{Mn}_{1-x}\text{O}_3$, the general formula is $\text{RE}^{3+}\text{Mn}^{4+}_{1-x}\text{Co}^{2+}_{1-x}\text{Co}^{3+}_{2x-1}\text{O}^{2-}_3$ (RE=rare-earth element) when the substitution at the manganese site exceeds 50%.¹⁸⁾ If we assume this valence state formula for $\text{TmMn}_{1-x}\text{Co}_x\text{O}_3$, then the average ionic radius of the 3d transition metal ions in $\text{TmMn}_{1-x}\text{Co}_x\text{O}_3$ decreases. This would qualitatively account for the decrease in the lattice parameters and the unit cell volume.

3.2 Magnetic properties

Figures 3 and 4 plot, respectively, the temperature dependences of the field-cooled (M_{FC}) and zero-field-cooled (M_{ZFC}) magnetization for the $0 \leq x \leq 0.4$ SSR samples¹⁴⁾ and the $0.5 \leq x \leq 0.9$ CP samples in a magnetic field of 250 Oe. The insets of Figs. 3 and 4 respectively show the mass fraction of the SSR samples and the temperature dependence of $\chi_{\text{FC}}^{-1} = H/M_{\text{FC}}$ for the CP samples above 20 K. M_{FC} increases ferromagnetically below 60 K with decreasing temperature for $0.1 \leq x \leq 0.7$. From $x=0.1$ to 0.5, M_{FC} increases, and then decreases from $x=0.5$ to 0.9. With increasing x , the mass fraction of the orthorhombic phase increases, as do M_{FC} and M_{ZFC} . A discrepancy is observed between M_{FC} and M_{ZFC} below about 160 K for $0.1 \leq x \leq 0.3$, where the hexagonal and orthorhombic phases coexist, and M_{FC} and M_{ZFC} exhibit different temperature dependences below about 60 K. M_{FC} and M_{ZFC} for $x \geq 0.5$, where the main phase is orthorhombic, are also different below about 60 K. The appearance of the orthorhombic phase induces a rapid increase in magnetization below 60 K. For $x=0.8$ and 0.9, there is no ferromagnetic increase, but a separation between M_{FC} and M_{ZFC} can be seen below about 60 K. We will discuss the temperature dependence of M_{FC} for the orthorhombic phase at low temperatures in more detail below.

The inverse susceptibility of $\text{TmMn}_{1-x}\text{Co}_x\text{O}_3$ ($0.5 \leq x \leq 0.9$) above 130 K, shown in the inset of Fig. 4, can be fitted as a linear function of temperature, that is, by the Curie-Weiss law:

$$\chi_{\text{FC}} = \frac{M_{\text{FC}}}{H} = \frac{C}{T - \Theta}, \quad (1)$$

where C is the Curie constant, Θ is the Weiss temperature, and H is the external magnetic field. C is related to the effective paramagnetic magnetic moment P_{eff} via

$$P_{\text{eff}}^2 = \frac{3Ck_{\text{B}}}{N\mu_{\text{B}}^2}, \quad (2)$$

where N is the number of magnetic atoms (Tm, Mn, Co) per gram, μ_{B} is the Bohr magneton,

and k_B is the Boltzmann constant. The values of P_{eff} and Θ , obtained from M_{FC} , are plotted in Fig. 5 as functions of x . It can be seen that Θ , which is about 15 K for $x=0.5$, decreases with increasing x and is negative for $x \geq 0.8$. It is found that ferromagnetic and antiferromagnetic interactions predominate for $x \leq 0.7$ and $x > 0.7$, respectively. P_{eff} also decreases with increasing x . Ghiasi et al. investigated the valence states of Mn and Co in $\text{LaMn}_{1-x}\text{Co}_x\text{O}_3$ nanoperovskites by X-ray absorption spectroscopy.¹⁹⁾ They found that $\text{LaMn}_{0.75}\text{Co}_{0.25}\text{O}_3$ contained Mn^{3+} , Mn^{4+} , and Co^{2+} , while $\text{LaMn}_{0.25}\text{Co}_{0.75}\text{O}_3$ contained Mn^{4+} , Co^{2+} , and Co^{3+} , and $\text{LaMn}_{0.5}\text{Co}_{0.5}\text{O}_3$ contained Mn^{3+} , Mn^{4+} , Co^{2+} , and Co^{3+} . To facilitate the discussion, we will again assume the following valence state formula for $\text{REMn}_{1-x}\text{Co}_x\text{O}_3$ for $x \geq 0.5$: $\text{RE}^{3+}\text{Mn}^{4+}_{1-x}\text{Co}^{2+}_{1-x}\text{Co}^{3+}_{2x-1}\text{O}^{2-}_3$. Among these ions, Co^{2+} and Co^{3+} can have $S=3/2$ (high spin, HS) or $S=1/2$ (low spin, LS), and $S=2$ (HS) or $S=0$ (LS) states, respectively. Assuming that the theoretical paramagnetic moments of Mn^{3+} , Mn^{4+} , and Co^{2+} are $7.57 \mu_B$, $3.87 \mu_B$, and $3.87 \mu_B$ (HS), respectively, at $x = 0.5$, P_{eff} equal to $6.01 \mu_B$ per atom is obtained for these magnetic atoms from Eq. (3):

$$P_{\text{eff}} = \sqrt{\frac{\sum p_i^2}{2}}. \quad (3)$$

The 2 in the dominator of Eq. (3) corresponds to the number of magnetic atoms in the formula $\text{TmMn}_{1-x}\text{Co}_x\text{O}_3$. This calculated P_{eff} is close to the experimental value. It is concluded from the P_{eff} value for $x=0.5$ that Co^{2+} must be HS. In Fig. 5, the x dependence of P_{eff} is also shown for Co^{3+} (HS) and Co^{3+} (LS). If the electronic state of Co^{3+} for $x > 0.5$ is HS, P_{eff} increases with x . This contradicts the experimental results shown in Fig. 5. The values of P_{eff} agree qualitatively with calculations in which Co^{2+} and Co^{3+} are assumed to be in the HS and LS states, respectively.

For $0.5 \leq x \leq 0.7$, both M_{FC} and M_{ZFC} increase ferromagnetically at $T_C \approx 58$ K with decreasing T . Since the ferromagnetic interaction is predominant for $0.5 \leq x \leq 0.7$, this increase in magnetization is considered to be due to the canted magnetic transition of the Mn and Co ions, as reported for other rare-earth manganese oxides. The maximum values of M_{FC} are observed between 25 and 35 K. M_{FC} decreases with decreasing T and shows negative values below $T_{\text{comp}} \approx 13$ K for $x=0.7$. No ferromagnetic increase in magnetization is seen for $x=0.8$ and 0.9 , although a small peak can be seen at about 44 K in M_{ZFC} for $x=0.8$. The discrepancy between M_{FC} and M_{ZFC} for $x=0.8$ and 0.9 is considered to be due to antiferromagnetic ordering or competition between ferromagnetic and antiferromagnetic interactions.

Another characteristic of the temperature dependence of M_{FC} below ~ 30 K for $0.5 \leq x \leq 0.7$ is the rapid decrease with decreasing T . A similar decrease in M_{FC} is seen in other rare-earth manganese oxides.^{18,20-23)} Such a rapid decrease in M_{FC} indicates spin reversal phenomena related to rare-earth ions. The M - H curves for $\text{TmMn}_{0.5}\text{Co}_{0.5}\text{O}_3$ prepared by the solid-state

reaction method showed a large high-field magnetic susceptibility even below 20 K, which suggests that Tm^{3+} ($J=6$) is paramagnetic even at low temperatures. According to Cooke et al.,²¹⁾ the temperature dependence of M_{FC} can be fitted using the equation

$$M_{\text{FC}} = M_{\text{Mn,Co}} + \frac{C_{\text{Tm}}(H+H_{\text{int}})}{T-\Theta_{\text{W}}} , \quad (4)$$

where $M_{\text{Mn,Co}}$ and H_{int} are the saturated moment and the internal field at the Tm sites due to the canted Mn-Co moment, respectively. C_{Tm} is the Curie constant for paramagnetic Tm^{3+} ions, Θ_{W} is the Weiss temperature, and H is the applied field, which is 250 Oe. The solid lines in Fig. 6 show that the temperature dependence of the magnetization below ~ 25 K can be well approximated using Eq. (4); the fitting parameters are listed in Table I. This successful model, which is based on a ferromagnetically ordered Mn-Co sublattice and a paramagnetic Tm sublattice, suggests that the negative internal field induced by the Mn-Co sublattice affects the Tm sublattice. It is considered that at low temperatures (below ~ 25 K), the Tm^{3+} spin is oriented in the direction opposite to H by H_{int} . Such spin inversion due to $3d$ transition metal elements and rare-earth elements seems to be common in perovskite-type oxides with the structure ABO_3 , although the crystallographic reasons why H_{int} acts antiferromagnetically on the rare-earth element A are unclear.

4. Conclusion

From the plots of mass fraction vs x (insets of Figs. 2 and 3), the CP method was clearly demonstrated to be more suitable than the SSR method for $0.5 < x \leq 0.9$. Thus, we achieved the substitution of Mn through CP, and obtained almost a single orthorhombic phase for $0.5 \leq x \leq 0.9$ in $\text{TmMn}_{1-x}\text{Co}_x\text{O}_3$.

At $T > T_{\text{C}} \approx 58$ K, $\text{TmMn}_{1-x}\text{Co}_x\text{O}_3$, in which the Tm^{3+} , Mn^{4+} , Co^{2+} , and Co^{3+} ions are paramagnetic, is also paramagnetic. From the data on the unit cell volume and the effective moment, it is concluded that Co^{2+} has a high spin state ($S=3/2$) and that Co^{3+} in $\text{TmMn}_{1-x}\text{Co}_x\text{O}_3$ remains a low-spin-state ion ($S=0$). At $T = T_{\text{C}}$, a canted magnetic transition occurs as a result of the interaction between Mn and Co, and the magnetization increases ferromagnetically with decreasing T . Below the temperature at which M_{FC} is maximized, the interaction between Mn and Co ions induces a negative internal field H_{int} at the Tm sites. H_{int} reorients the Tm^{3+} spin in the direction opposite to the external field H . The total magnetization at low temperatures is explained on the basis of a two-sublattice model.

Acknowledgment

The authors would like to thank Prof. Hiroshi Isoda for his assistance with sample preparation.

References

- 1) T. Kimura, T. Goto, H. Shintani, K. Ishizuka, T. Arima, and Y. Tokura, *Nature* **426**, 55 (2003).
- 2) T. Goto, T. Kimura, G. Lawcs, A. P. Ramircz, and Y. Tokura, *Phys. Rev. Lett.* **92**, 257201 (2004).
- 3) J. Barrier, D. Meier, K. Berggold, J. Hemberger, A. Balbashov, J. A. Mydosh, and T. Lorenz, *Phys. Rev. B* **73**, 100402(R) (2006).
- 4) J. R. Sahu, A. Ghosh, A. Sundaresan, and C. N. R. Rao, *Mater. Res. Bull.* **44**, 2123 (2009).
- 5) K. Asai, K. Fujiyoshi, N. Nishimori, Y. Satoh, Y. Kobayashi, and M. Mizoguchi, *J. Phys. Soc. Jpn.* **67**, 4218 (1998).
- 6) D. O'Flynn, C.V. Tomy, M. R. Lees, A. Daoud-Aladine, and G. Balakrishnan, *Phys. Rev. B* **83**, 174426 (2010).
- 7) V. L. Joseph Joly, P. A. Joy, and S. K. Date, *Solid State Commun.* **121**, 219 (2002).
- 8) J. Hemberger, F. Schrettle, A. Pimenov, P. Lunkenheimer, V. Yu. Ivanov, A. A. Mukhin, A. M. Balbashov, and A. Loidl, *Phys. Rev. B* **75**, 035118 (2007).
- 9) N. Iwata and K. Kohn, *J. Phys. Soc. Jpn.* **67**, 3318 (1998).
- 10) K. Yoshii and H. Abe, *J. Solid State Chem.* **165**, 131 (2002).
- 11) H. A. Salama and G. A. Stewart, *J. Phys.: Condens. Matter* **21**, 386001 (2009).
- 12) V. Yu Pomjakushin, M. Kenzelmann, A. Dönni, A. B. Harris, T. Nakajima, S. Mitsuda, M. Tachibana, L. Keller, J. Mesot, H. Kitazawa, and E. Takayama-Muromachi, *New J. Phys.* **11**, 043019 (2009).
- 13) H. A. Salama, G. A. Stewart, W. D. Hutchison, K. Nishimura, D. R. Scott, and H. StC. O'Neill, *Solid State Commun.* **150**, 289 (2010)
- 14) T. Tanaka, A. Kumagai, Y. Amakai, N. Momono, S. Murayama, and H. Takano, *J. Korean Phys. Soc.* **63**, 546 (2013).
- 15) C. Morilla-Santos, L. B. Arruda, C. A. Silva, and P. N. Lisboa-Filho, *J. Electroceram.* **27**, 215 (2011).
- 16) C. Moure, D. Gutierrez, J. Tartaj, and P. Duran, *J. Eur. Ceram. Soc.* **23**, 729 (2003).
- 17) F. Izumi and K. Momma, *Solid State Phenom.* **130**, 15 (2007).
- 18) O. Peña, A. B. Antunes, M. N. Baibich, P. N. Lisboa-Filho, V. Gil, and C. Moure, *J. Magn. Magn. Mater.* **312**, 78 (2007).

- 19) M. Ghiasi, M. U. Delgado-Jaime, A. Malekzadeh, R. P. Wang, P. S. Miedema, M. Beye, and F. M. F. de Groot, *J. Phys. Chem. C* **120**, 8167 (2016).
- 20) G. Demazeau, M. Pouchard, and P. Hagenmuller, *C. R. Acad. Sci. Ser. C* **277**, 109 (1973) [in French].
- 21) A. H. Cooke, D. M. Martin, and M. R. Wells, *J. Phys. C: Solid State Phys.* **7**, 3133 (1974).
- 22) J. Hemberger, S. Lobina, H. -A. Krug von Nidda, N. Tristan, V. Yu. Ivanov, A. A. Mukhin, A. M. Balbashov, and A. Loidl, *Phys. Rev. B* **70**, 024414 (2004).
- 23) Bibhuti B. Dash and S. Ravi, *J. Magn. Magn. Mater.* **429**, 281 (2017).

Figure Captions

Table I Fitting parameters for M_{FC} for $x = 0.5, 0.6,$ and 0.7 .

Fig. 1. (Color online) X-ray diffraction patterns for various $TmMn_{1-x}Co_xO_3$ samples. The XRD pattern for Tm_2O_3 , which is considered an impurity, is shown at the top as a reference.

Fig. 2. (Color online) Lattice parameters and unit cell volume as functions of x . The open symbols were obtained from Ref. 19. The inset plots mass fraction vs x . All these values, except for those for $x=0$, were obtained from samples prepared by complex polymerization.

Fig. 3. (Color online) Temperature dependences of field-cooled (FC, filled symbols) and zero-field-cooled (ZFC, open symbols) magnetizations for $TmMn_{1-x}Co_xO_3$ for $0.0 \leq x \leq 0.4$, which were prepared by the solid-state reaction. The inset plots mass fraction vs x for samples prepared by the solid-state reaction.

Fig. 4. (Color online) Temperature dependences of field-cooled (FC, filled symbols) and zero-field-cooled (ZFC, open symbols) magnetizations for $TmMn_{1-x}Co_xO_3$ for $0.5 \leq x \leq 0.9$.

Fig. 5. (Color online) Effective paramagnetic moment P_{eff} and Weiss temperature Θ as functions of x for $TmMn_{1-x}Co_xO_3$. The filled (open) symbols are the experimental (calculated) P_{eff} data for the two-spin states of Co^{3+} .

Fig. 6. (Color online) Temperature dependence of M_{FC} for $x = 0.5$ to 0.7 . The solid lines below 25 K are fits using Eq. (4).

Table I Fitting parameters for M_{FC} for $x = 0.5, 0.6,$ and 0.7 .

Co concentration x	$M_{Mn,Co} / \text{emu g}^{-1}$	$H_{\text{int}} / \text{kOe}$	Θ_w / K
0.5	7.8	-4.0	-11
0.6	4.0	-3.0	-14
0.7	1.8	-2.1	-13

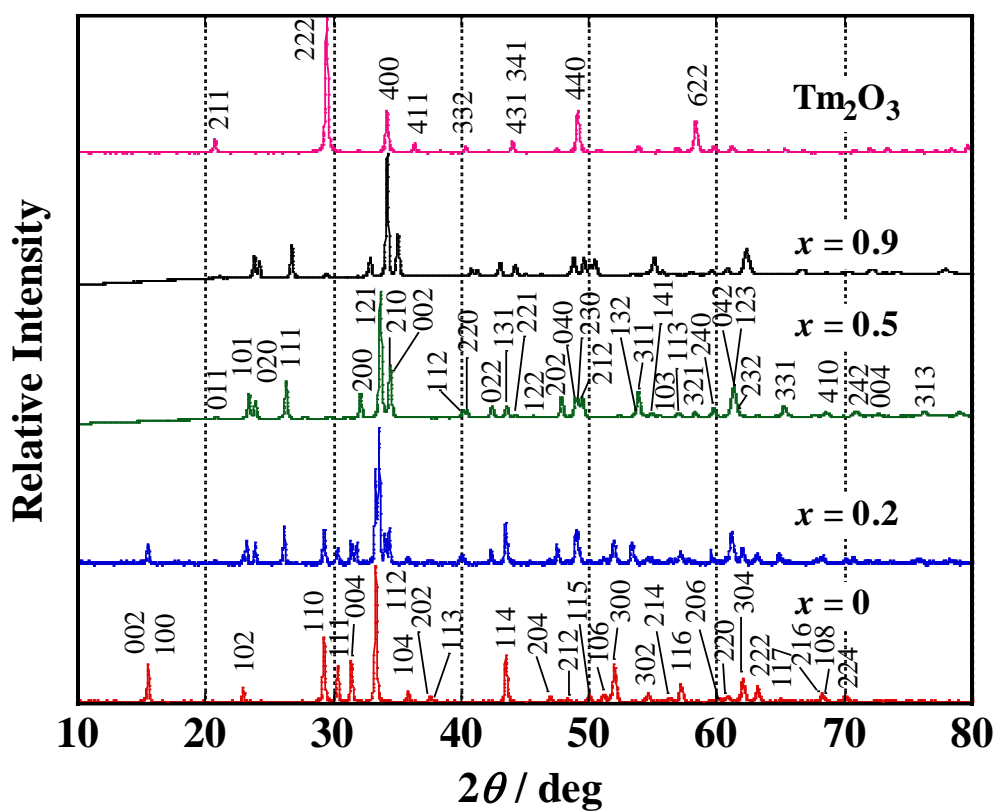


Fig. 1. (Color online) X-ray diffraction patterns for various $\text{TmMn}_{1-x}\text{Co}_x\text{O}_3$ samples. The XRD pattern for Tm_2O_3 , which is considered an impurity, is shown at the top as a reference.

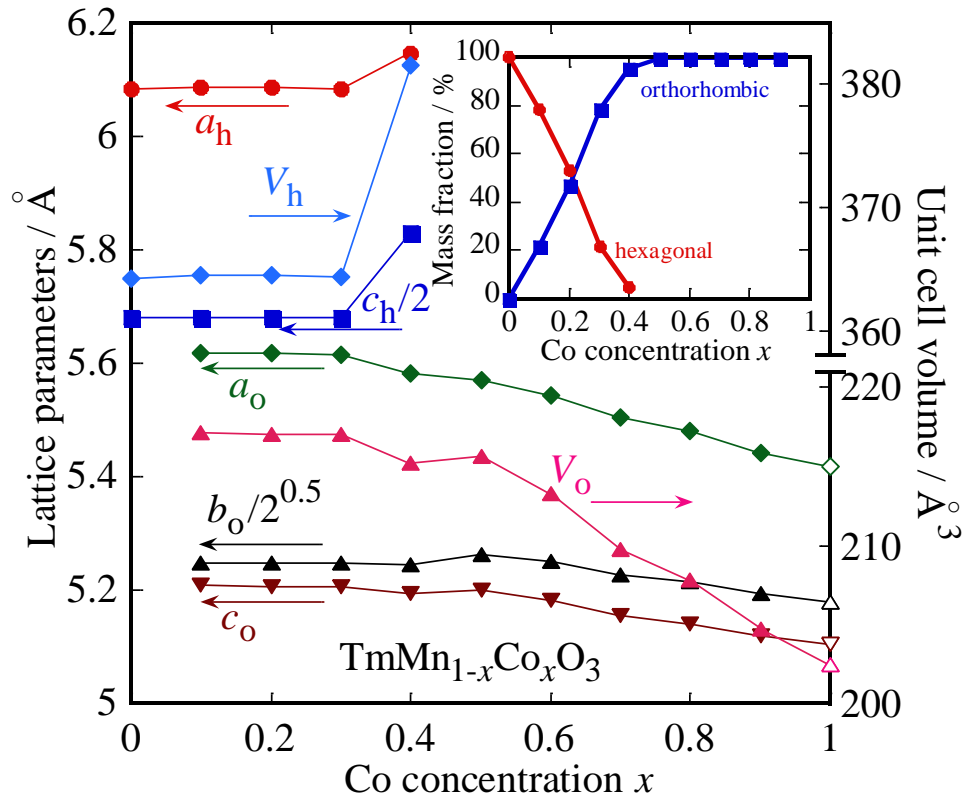


Fig. 2. (Color online) Lattice parameters and unit cell volume as functions of x . The open symbols were obtained from Ref. 19. The inset plots mass fraction vs x . All these values, except for those for $x=0$, were obtained from samples prepared by complex polymerization.

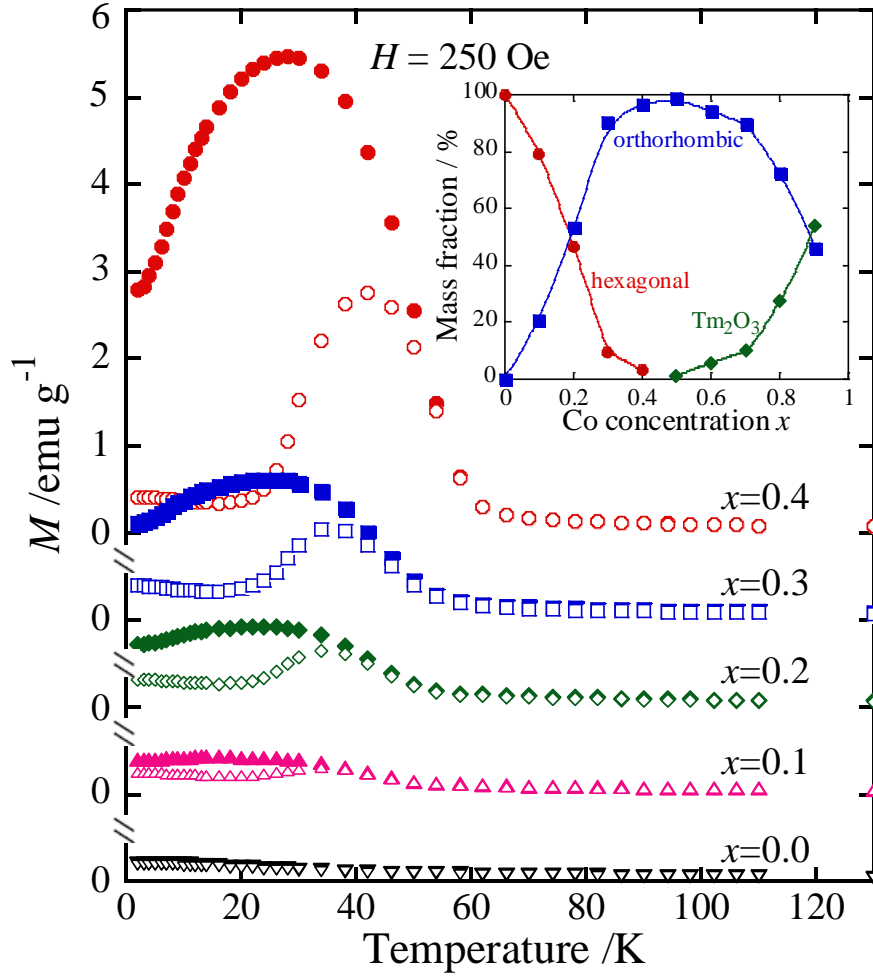


Fig. 3. (Color online) Temperature dependences of field-cooled (FC, filled symbols) and zero-field-cooled (ZFC, open symbols) magnetizations for $\text{TmMn}_{1-x}\text{Co}_x\text{O}_3$ for $0.0 \leq x \leq 0.4$ prepared by the solid-state reaction. The inset plots mass fraction vs x for samples prepared by the solid-state reaction.

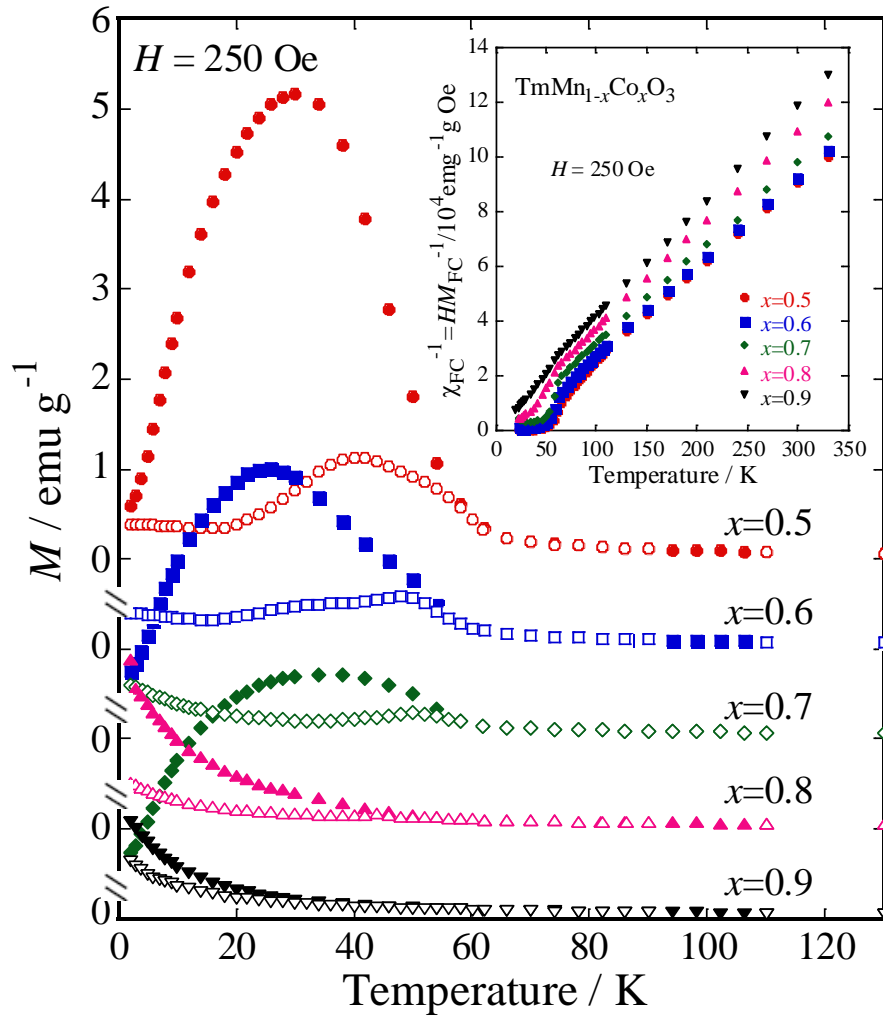


Fig. 4. (Color online) Temperature dependences of field-cooled (FC, filled symbols) and zero-field-cooled (ZFC, open symbols) magnetizations for $\text{TmMn}_{1-x}\text{Co}_x\text{O}_3$ for $0.5 \leq x \leq 0.9$.

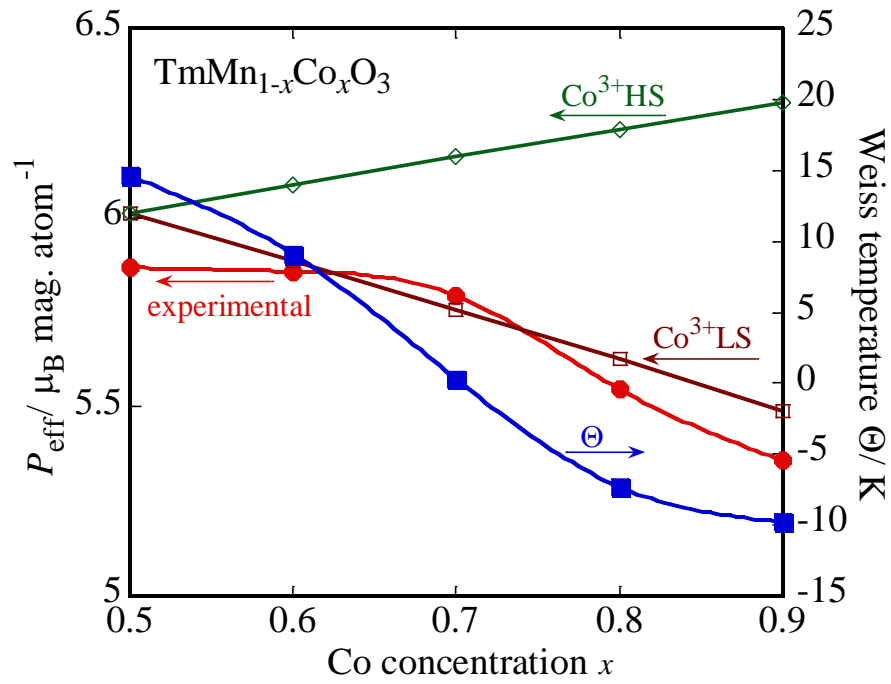


Fig. 5. (Color online) Effective paramagnetic moment P_{eff} and Weiss temperature Θ as functions of x for $\text{TmMn}_{1-x}\text{Co}_x\text{O}_3$. The filled (open) symbols are the experimental (calculated) P_{eff} data for the two spin states of Co^{3+} .

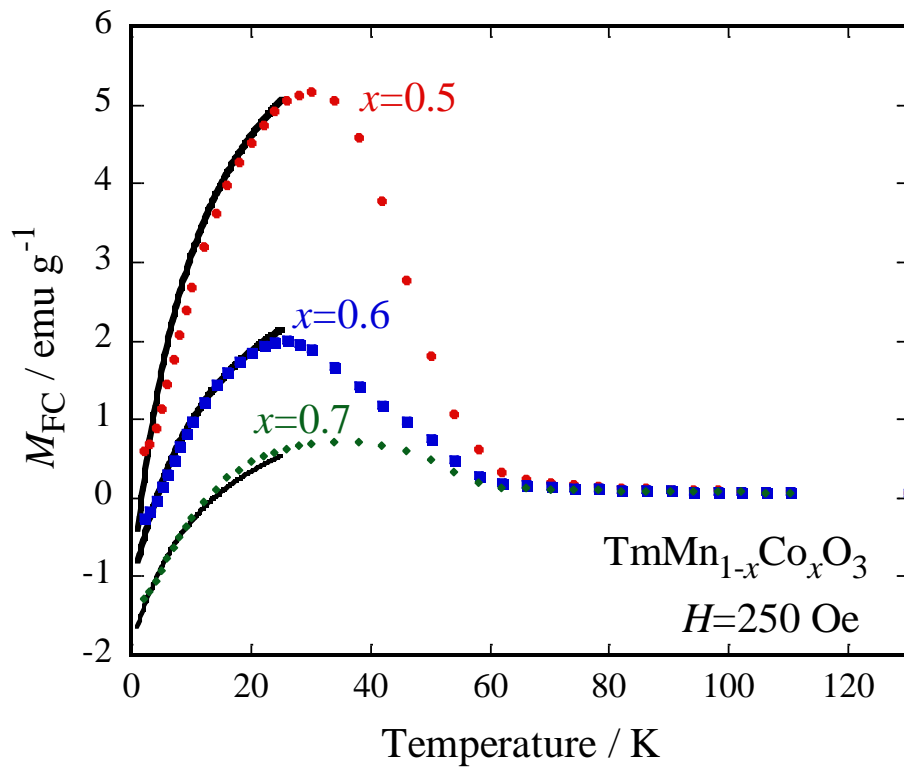


Fig. 6. (Color online) Temperature dependence of M_{FC} for $x = 0.5$ to 0.7 . The solid lines below 25 K are fits obtained using Eq. (4).